Applied Surface Science 679 (2025) 161205

Contents lists available at ScienceDirect

Applied Surface Science

journal homepage: www.elsevier.com/locate/apsusc

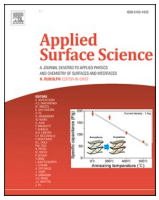

Full Length Article

Synergistic adsorption-photocatalytic remediation of methylene blue dye from textile industry wastewater over NiFe LDH supported on tyre-ash derived activated carbon

Tshimangadzo S. Munonde [a,*], Ntakadzeni Madima [b,*], Rudzani Ratshiedana [a], Philiswa Nosizo Nomngongo [c], Lethula E. Mofokeng [d], Ratshilumela S. Dima [e]

[a] Institute for Nanotechnology and Water Sustainability, College of Science, Engineering, and Technology, University of South Africa, Florida Science Campus, Roodepoort, 1710, South Africa
[b] Advanced Materials Division, Mintek, Private Bag X3015, Randburg, 2125, Gauteng Province, South Africa
[c] Department of Chemical Sciences, University of Johannesburg, Doornfontein Campus, P.O. Box 17011, Doornfontein, 2028, South Africa
[d] Department of Chemistry, Faculty of Natural and Agricultural Sciences, University of Pretoria, Private Bag X20, Hatfield 0028, Pretoria, South Africa
[e] Next Generation Enterprises and Institution Cluster, Council for Scientific and Industrial Research, P.O. Box 395, Pretoria 0001, South Africa

ARTICLE INFO

Keywords:
Methylene Blue
Adsorption
Photocatalysis
NiFe LDH/Activated Carbon
Degradation
Textile Wastewater

ABSTRACT

The photocatalytic performance of the multilayered NiFe LDH/Activated Carbon was evaluated for the degradation of methylene blue (MB) in industrial textile wastewater, considering prior adsorption on the photocatalyst surface. The XRD, XPS, BET, TEM and FE-SEM results confirmed that the highly exposed mesoporous layers, carbon backbone, and interlayer anions serve as active sites responsible for the adsorption of MB dye due to the expected electrostatic interactions. Electrochemical methods such as CV, LSV and EIS revealed the improved conductivity and supported the interactions observed. Encouraged by these interactions, the irradiation of visible light enabled the degradation of methylene blue, and the degradation products were monitored using UPLC chromatograms and MS spectra. The removal efficiencies of the MB dye were found to be 17.5 %, 51.2 %, 67.1 %, 84.8 %, and 94.2 % due to photolysis, adsorption, and degradation on AC, NiFe LDH nanosheets, and NiFe LDH/AC nanocomposite, respectively. The results of the UPLC chromatograms and MS spectra suggested that MB was mineralized into simpler fragments after 30 min of visible light irradiation. Scavenging studies were examined using a series of scavenging agents. However, the maximum photodegradation was attained in the absence of the scavengers. The reusability studies showed that the MB photodegradation efficiency declined by 20.8 %, possibly due to the loss of the catalyst during the washing step. Nonetheless, the NiFe LDH/AC structure remained intact, suggesting the strong stability of the photocatalyst. The plausible degradation mechanism and probable degradation pathway of MB were outlined and supported by the chromatographs and MS results. The overall results suggest that photocatalysis of cationic dyes such as MB on NiFe LDH/AC should be encouraged to work towards sustainable solutions for textile water treatment.

1. Introduction

Industrial wastewater management is critical to advance global environmental protection goals, as well as to contribute to sustainable development goals [1]. This can be achieved through the removal or reduction of contaminants from influent wastewater to obtain a final effluent that is free of contaminants or has reduced contaminants to within acceptable concentrations [2–4]. Subsequently, only 1 % of the surface water of the Earth is available as potable water and suitable for human consumption, although more than 70 % is present [5,6]. An assortment of persistent organic and inorganic contaminants with varying degrees of toxicity, carcinogenicity, and mutagenicity are the main causes of water pollution [7,8]. Organic dyes are among the many different types of organic contaminants that end up in water bodies. Due to their poisonous nature, both people and the ecosystem are at risk. They have a complicated molecular structure and may withstand heat

* Corresponding authors.
E-mail addresses: munonts@unisa.ac.za (T.S. Munonde), ntakadzenim@mintek.co.za (N. Madima), ratshr@unisa.ac.za (R. Ratshiedana), pnnomngongo@uj.ac.za (P. Nosizo Nomngongo), sdima@csir.co.za (R.S. Dima).

https://doi.org/10.1016/j.apsusc.2024.161205
Received 26 June 2024; Received in revised form 17 August 2024; Accepted 7 September 2024
Available online 12 September 2024

and detergents [9]. The most prevalent organic dye discovered in wastewater is methylene blue (MB), mainly due to their widespread use in a diversity of industries, such as food, paper, plastic, leather, and textiles [10]. It was discovered that even at very low concentrations, the prevalence of MB in water bodies can have detrimental impacts on human health, causing diseases such as elevated blood pressure, headaches, nausea, and throat irritation [10,11]. Therefore, it is now urgently necessary to address the contamination caused by the methylene blue dye.

Taking into account the above, sophisticated methods such as membrane separation, chemical oxidation, adsorption, coagulation, chemical precipitation, and photocatalysis have been developed to counteract the devastating hazards associated with the presence of MB in water [12–16]. Although adsorption has been reported for the decolorization of MB dye, this does not always translate into the mineralization of organic pollutants [17]. This requires the degradation of MB for complete mineralization after adsorption in the photocatalyst, as photocatalysis has the unique advantage of converting toxic to nontoxic components such as water (H_2O), carbon dioxide (CO_2) and nitrogen (N_2), among others [18]. This work concentrates on the integration of adsorption and photocatalysis as MB remediation strategies, as these approaches are low-cost, highly effective and environmentally benign [19,20]. However, finding appropriate materials that have strong catalytic performances and significant adsorption capacity is necessary for the implementation of such a process. To tackle this, different strategies can be used, such as enhancing the adsorption capabilities of well-known catalytic materials or giving well-known catalytic functionalities of adsorbents [21]. Consequently, researchers worldwide have focused exclusively on developing efficient adsorbent-catalytic materials for the simultaneous adsorption and photocatalytic degradation of organic dyes.

Methylene blue has been decolorized and degraded by titanium-based photocatalysts. However, one of the primary disadvantages linked to the utilization of titanium dioxide (TiO_2) photocatalysts is the elevated energy requirement linked to UV light stimulation [22–25]. To curb this, a variety of materials have been studied as photocatalysts for MB degradation; however, these are still limited by high-energy demand and longer degradation times. Interestingly, NiFe layered double hydroxide (NiFe LDH) has advanced as a potential photocatalyst for the mineralization of organic dyes due to their stimulating surface chemistry [26,27]. For instance, previous studies by Lei *et al.* (2017) [28] and Lu *et al.* (2016) [29] have shown that NiFe LDH materials have a significant adsorption capacity for various dyes, a few of which are Congo red (205–330 mg g^{-1}) and methyl orange (205.76 mg g^{-1}). The adsorption followed a Langmuir type of isotherm and pseudo-second-order kinetics, indicating monolayer formation and the chemical nature of the process. However, the adsorption of these dyes on LDHs has been criticized for causing secondary pollution after their desorption [30]. Nonetheless, the tunable composition, anion exchange capability, and exceptional stability of LDHs enable them to show potential for dye degradation and catalytic operations. For instance, Nayak and Parida [31] fabricated NiFe LDH/N-rGO/g-C_3N_4 heterostructure which performed superiorly towards the photocatalytic activities of Rhodamine B (RhB) and phenol reaching 95 % and 72 % mineralization, respectively. However, the study only degraded RhB and phenol in synthetic wastewater and was not applied to real textile wastewater, and the resultant degradation products were not thoroughly investigated. Furthermore, the highest degradation was achieved in a long period of 2 h, suggesting the more use of energy. As such, due to their limited conductivity resulting from the extensive stacking of the layers, the performance of NiFe LDH in organic dyes adsorption and degradation is limited, particularly in real textile wastewater, as they often demand intensive high energy and longer degradation times [18]. On the other hand, NiFe LDH integrated with nanocarbon has been reported to improve the conductivity, thus limiting the high energy demand and longer degradation times for photocatalysis [32–34].

Following these deliberations and identified gaps, this study employs a visible light active NiFe LDH nanomaterial that has been supported on tyre-ash derived activated carbon (AC) to move the absorption edge towards the visible light to systematically investigate the photocatalysis process in textile wastewater. By combining adsorption-photocatalysis, effective methylene blue remediation in textile wastewater using NiFe LDH supported on tyre ash-derived activated carbon was realized. The results suggest that NiFe LDH/AC was a suitable photocatalyst for the degradation of methylene blue into less toxic by-products identified using Ultra Performance Liquid Chromatography (UPLC) and Mass spectroscopy (MS spectra).

2. Experimental

2.1. Reagents and materials

To prepare solutions, ultrapure deionized water was utilized throughout, and all the chemicals used were of analytical grade. Ferric nitrate ($Fe(NO_3)_3{\cdot}9H_2O$), nickel nitrate hexahydrate ($Ni(NO_3)_2{\cdot}6H_2O$), urea ($CO(NH_2)_2$), ethylene glycol ($(CH_2OH)_2$), absolute ethanol (CH_3CH_2OH), acetic acid (CH_3COOH, 99 %), nitric acid (HNO_3, 68 %), hydrogen peroxide (H_2O_2, 30 %), and methylene blue dye were obtained from Sigma-Aldrich, South Africa. Ascorbic acid (AA), formic acid (FA), and isopropanol (IPA) were also purchased from Sigma-Aldrich, South Africa.

2.2. Synthesis of activated carbon from waste tyre-ash

Activated carbon derived from waste tyre was prepared using a previously modified method [35]. Concisely, the collected waste tyre was cut into small pieces and washed with water prior to pyrolysis on a quartz tube placed in an electric tubular furnace at 900 °C under N_2 purging (2 mL min^{-1}). Subsequently, the pyrolyzed product was subjected to a chemical activation method, where hydrogen peroxide (H_2O_2) was used as the activating agent heated in Teflon vessels in a microwave system for the activation process. Different power intensities of 300 W and 600 W were applied at a constant irradiation time of 15 min and an established ratio of 1:10 (m/m) for pyrogenised carbon/H_2O_2.

2.3. Synthesis of NiFe LDH supported on activated carbon (NiFe LDH/AC)

Following the successful preparation of activated carbon, NiFe LDH/AC was then prepared using the Hydrothermal method proposed previously with slight modifications [36]. In summary, 1.16 g Fe$(NO_3)_3{\cdot}9H_2O$ and 4.66 g $Ni(NO_3)_2{\cdot}6H_2O$ were dissolved in 20 mL of deionized water whilst stirring for 20 min. Subsequently, 1.14 g of activated carbon was added, with 3.46 g of urea added afterwards and stirring was allowed to continue for a further 30 min. Thereafter, the obtained slurry was transferred into a Teflon-lined autoclave where it was heated at 120 °C for 18 h. Afterwards, the autoclave was cooled to room temperature, and the product was washed thoroughly using deionized water (100 mL) and ethanol (20 mL). The final product was dried for 12 h in an oven at 100 °C before being ground into a fine powder using a pestle and mortar. The same method was followed for the synthesis of NiFe LDH, but the step for the addition of AC was excluded. The reaction mechanism is outlined in equations (1–3) below.

3. The reaction mechanism for the formation of NiFe LDH

$$CO(NH_2)_2 + 3H_2O \rightarrow 2OH^- + 2NH_4^+ + CO_2 \quad (1)$$

$$CO_2 + H_2O \rightarrow CO_3^{2-} + 2H^+ \quad (2)$$

$$Ni^{2+} + Fe^{3+} + OH^{-} + CO_3{}^{2-} \rightarrow \text{NiFe LDH} - CO_3{}^{2-} \quad (3)$$

Under heat, urea in solution breaks down into carbon dioxide (CO_2) and ammonia ions $(NH_4)^+$ (equation (1). The carbonate ion (CO_3^{2-}) is created when the excess carbon dioxide (CO_2) in the reactor hydrolyzes and reacts with the water (equation (2). After that, in order to balance the excess positive charge, Ni and Fe interact with the hydroxyl (OH^-) and CO_3^{2-} ions in solution to form the NiFe LDH with intercalated CO_3^{2-} anions (equation (3) [36].

3.1. Characterization Techniques

To examine the crystalline structure of the synthesized samples, the X-ray diffraction (XRD) measurements were conducted on a PANalytical X'Pert X-ray Diffractometer (PANalytical BV, Netherlands). The measurement utilized Cu Kα radiation (λ = 0.15406 nm) in the 2θ range 4–80°. Using the PerkinElmer Spectrum 100 (Waltham, MA, USA), Fourier-transform infrared spectroscopy (FTIR) was utilized to analyze the functional groups present in the synthesized samples. The analysis covered the wavenumber range of 4000 to 400 cm^{-1}. Field Emission Scanning Electron Microscope (FESEM, Auriga Cobra FIB FE-SEM, Germany) and High-Resolution Transmission Electron Microscope (HR-TEM, JEOL 2100, Japan) were utilized to study the morphological properties of the as-synthesized catalysts. FESEM was coupled with Energy Dispersive X-ray Spectroscopy (EDX) to give information on the elemental compositions of as-synthesized catalysts, and this was done at an accelerating voltage of 20 kV. X-ray photoelectron spectroscopy (XPS, Thermo ESCALAB 250Xi) was utilized for the determination of the elemental composition and valence state of the as-synthesized catalysts. N_2 adsorption–desorption measurements were performed at a temperature of 77 K to ascertain the surface area, pore volume, and pore diameter using a Tristar II instrument (Micromeritics, Norcross, GA, USA). Before analysis, the as-synthesized catalysts were degassing at 393 K for 8 h. The UV–Vis absorption spectra of the as-prepared catalysts were measured on a UV spectrophotometer (PerkinElmer UV–Vis spectrometer Lambda 650). The band gap energies of the catalysts were estimated using Tauc's plot.

3.2. Adsorption-Photocatalytic experiment

The effectiveness of the synthesized NiFe LDH/AC nanocomposite in terms of adsorption (Ads) and photocatalytic degradation (PD) was evaluated by tracking the removal efficiency of methylene blue (MB), a contemporary dye pollution. In a typical process, 100 mL of 30 mg L^{-1} dye concentration was used with 30 mg of catalyst (**Table S1** shows the optimization of the pH, mass, concentration and time, with the optimum conditions for each parameter selected from the table). The solution was subjected to adsorption for 30 min at room temperature (24.7℃ within 30 min adsorption), before photocatalytic degradation. After 30 min of adsorption, the solution was then exposed to SynLED Parallel Photoreactor 2.0 with bottom-lit LEDs (450 nm) in a 4x4 reaction block array that provides a consistent light intensity (320 lm) and produces a visible light intensity of 100 mW cm^{-2}. The temperature was monitored from the initial temperature of 24.7℃ which was capped at 30, 40, 50 and 60℃, with the temperature of 50℃ selected as the optimum temperature due to high degradation rates achieved (**Fig. S1**). During both adsorption and photocatalytic degradation using the optimum conditions, 2 mL of the mixture was withdrawn at given time intervals amounting to a maximum of 30 min, and the catalyst was separated from the solution by centrifugation. Through the aid of a UV–Vis spectrophotometer, the aliquots were used to assess the intensity of the MB absorption peak (664 nm) at a certain time. The following equation was used to determine the removal efficiency (Equation (4):

$$Removalefficiency = \left(1 - \frac{A}{A_o}\right) \times 100 \quad (4)$$

Where A is the maximum dye absorbance at a certain time and A_o is the initial dye absorbance. The linearity of the pseudo-first-order process was plotted for the photocatalytic degradation kinetics investigation using the following Equation (5):

$$-\ln\left(\frac{A}{A_o}\right) = k_{app}t - \ln\left(\frac{A}{A_o}\right) = k_{app}t \quad (5)$$

Where $k_{app,}$ is the apparent rate constant, and t is the irradiation time. Furthermore, to assess the stability and reusability of NiFe LDH/AC, the catalyst was retrieved and utilized under the same circumstances in the next round of photocatalytic degradation tests. Following each cycle, the sample was centrifuged, washed with distilled water, and then dried in a heating oven at 100℃ for 10 h. In five consecutive experimental cycles, different variations in the deteriorating process were investigated.

3.3. Sample collection

Pre-cleaned plastic containers were used to collect the influent and effluent textile wastewater from a KwaZulu-Natal textile factory. The containers were then kept cold until examination. In the influent and effluent textile wastewater, MB concentrations were determined to be 6.17 mg L^{-1} and 2.33 mg L^{-1}, respectively. In terms of river water collected, the concentrations of MB were found to be 1.19 mg L^{-1} and 2.64 mg L^{-1} for upstream and downstream, respectively.

4. Results and discussion

4.1. Characterization

4.1.1. XRD and FTIR analysis

The XRD patterns of AC and NiFe LDH/AC nanocomposites were conducted to examine the crystalline structure of the synthesized catalysts and the results are demonstrated in Fig. 1(a and b). As observed in Fig. 1**(a)**, the activated carbon pattern displayed an amorphous halo-centered peak at 2θ = 24.5°. This halo is associated with the (002) plane's reflection, characteristic of non-crystalline materials like activated carbon [37]. For NiFe LDH/AC demonstrated in Fig. 1**(b)**, the diffraction peaks were observed at 2θ = 11.3°, 22.3°, 33.1°, 34.3°, 35.2°, 38.3°, 46.3°, 60.9° and 61.1° (JCPDS No. 38–0715) were observed, corresponding to the crystal planes (003), (006), (101), (012), (009), (015), (018), (110), and (113), respectively [36,38]. The interlayer d spacing was calculated to be 0.775 nm on the plane (003) using Bragg's law. To further study the presence of functional groups on the surface of as-synthesized AC and NiFe LDH/AC nanocomposites, the FTIR analysis was conducted. As illustrated in Fig. 1**(b)**, both FTIR spectra exhibited absorption bands at 3400 and 1629 cm^{-1} due to the stretching vibration of the hydroxyl groups and the bending vibration of the interlayer H_2O, respectively. The vibrations of the intercalated carbonate anion were observed in both spectra and were responsible for the absorption band around 1358 cm^{-1} [38]. The interaction between the metal hydroxide layers and the interlayer anion was identified to be responsible for the 700 cm^{-1} band in the FTIR spectrum of the NiFe LDH/AC nanocomposite. Furthermore, the vibration of M−O or M−O−M (M=Fe and Ni) was the primary cause of the band at 620 cm^{-1} [39,40].

4.1.2. BET analysis

The surface characteristics of the NiFe LDH nanosheets, activated carbon (AC), and the modified NiFe LDH/AC nanocomposite were evaluated using the N_2 adsorption–desorption isotherms shown in Fig. 2. In Fig. 2**(a),** AC showed type IV isotherm with H1-type hysteresis loop indicating the presence of microporous (<2 nm) and mesoporous (2–50

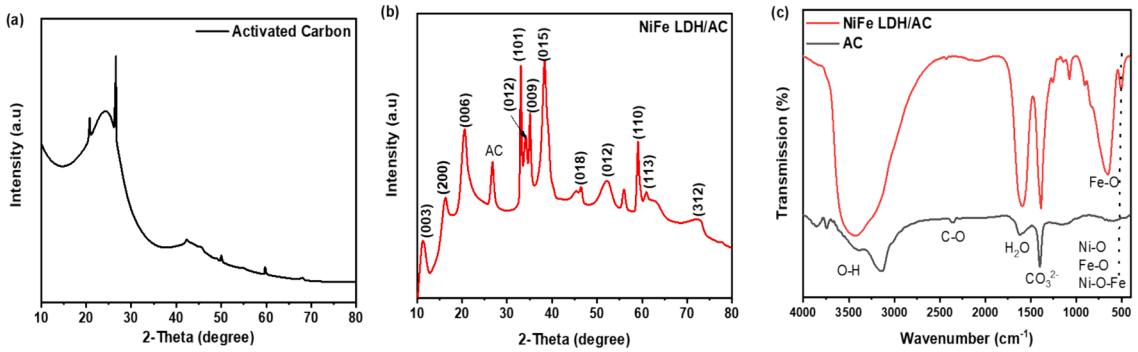

Fig. 1. (a and b) XRD pattern, (c) FITR spectra of Activated Carbon (AC), and NiFe LDH/AC nanocomposites.

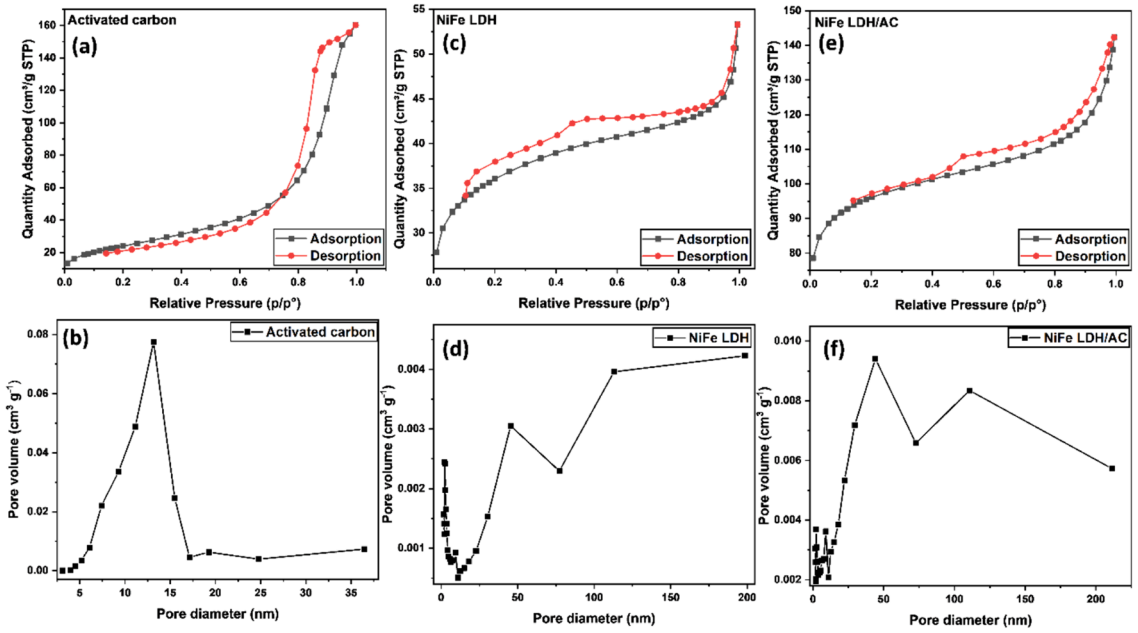

Fig. 2. BET analysis and the corresponding pore distribution plots of (a and b) activated carbon (AC), (c and d) NiFe LDH nanosheets, and (e and f) NiFe LDH/AC nanocomposite.

nm) pores, however, micropores were more dominant [41]. Both the NiFe LDH nanosheets and the modified NiFe LDH/AC nanocomposite display a type IV isotherm with an H3-type hysteresis loop, which implies the presence of mesopores (as shown in Fig. 2**(b-c)**. This was supported by inset pore distribution graphs showing pore sizes in the range of mainly 2–50 nm. At the same time, some were macroporous (>50 nm) in accordance with the evaluations of porous materials by the International Union of Pure and Applied Chemistry (IUPAC) [42]. Table 1 provides a more comprehensive summary of the surface attributes. It is evident that following surface modification with AC, the NiFe LDH nanosheets' BET surface area increased from 54.3 $m^2\ g^{-1}$ to 141.2 $m^2\ g^{-1}$. The surface grafting of NiFe LDH nanosheets onto AC greatly enhanced the surface chemistry of the resulting NiFe LDH/AC nanocomposite. This was demonstrated by the surface-improved NiFe LDH/AC nanocomposite, which also showed an increased pore size and pore volume compared to those of the NiFe LDH nanosheets.

Table 1
BET properties of NiFe LDH nanosheets, activated carbon (AC), and NiFe LDH/AC nanocomposite.

Surface properties	Activated carbon	NiFe LDH nanosheets	NiFe LDH/AC nanocomposite
BET surface area ($m^2\ g^{-1}$)	157.9	54.3	141.2
Average pore size (nm)	8.2	12.3	20.7
Total pore volume ($cm^3\ g^{-1}$)	0.17	0.34	0.62

4.1.3. Morphology analysis

The field emission scanning electron microscopy (FE-SEM) and high-resolution transmission electron microscopy (HR-TEM) were used to examine further the morphology and microstructure of the as-prepared NiFe LDH/AC nanocomposite. The nanocomposite showed a typical nanoflower-sphere-like shape with many radially organized NiFe-LDH nanosheets, as observed in the FE-SEM image of NiFe LDH/AC nanocomposite shown in Fig. 3(a and b). The open space between the nanosheets is anticipated to improve the mobility of electrons and holes during photocatalysis, and the porous structure is expected to offer a large number of active sites for pollutant adsorption [36]. Furthermore, as shown in Fig. 3**(c)**, HR-TEM was used to assess the interior morphology of the NiFe LDH/AC nanocomposite. NiFe LDH multilayers supported on sheets of activated carbon are visible in the HR-TEM image. For elemental composition, the existence of Ni, Fe, O, and C in NiFe LDH/AC nanocomposite was verified by the EDX spectrum, as illustrated in Fig. 3**(d)**.

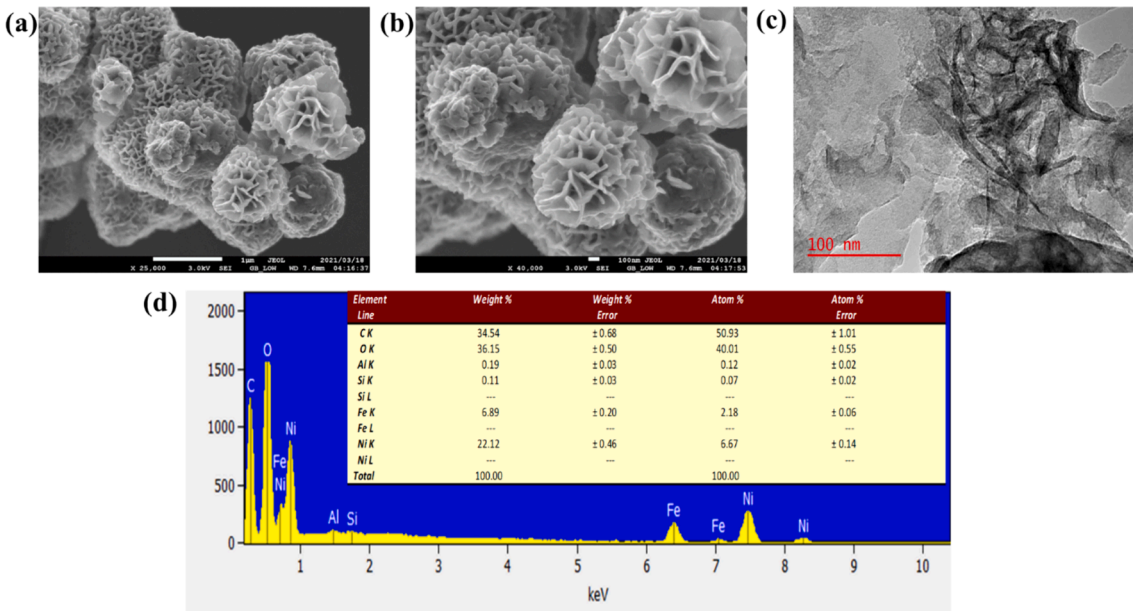

Fig. 3. (a and b) FE-SEM images, (c) HR-TEM image and (d) EDX spectrum, of NiFe LDH/AC nanocomposite.

4.1.4. XPS analysis

As shown in Fig. 4**,** X-ray photoelectron spectroscopy (XPS) of NiFe LDH nanosheets, AC, and the modified NiFe LDH/AC nanocomposite is used to study the chemical composition and detailed chemical state of the photocatalyst surface [40]. The XPS survey spectrum agrees well with the EDX results by showing the existence of Ni, Fe, O, and C in the NiFe LDH/AC nanocomposite. The high-resolution energy spectrum of N 2p exhibits peaks at binding energies of 856.5 and 879.8 eV due to spin–orbit doublets of Ni $2p_{3/2}$ and Ni $2p_{1/2}$, respectively. Additionally, two shake-up satellite peaks were observed, indicating that Ni^{2+} exists in a state of high spin [43]. In the high-resolution Fe 2p spectrum, two peaks located at 712.6 eV and 725.7 eV are observed due to Fe $2p_{3/2}$ and Fe $2p_{1/2}$, respectively, along with two satellite peaks indicating the existence of Fe^{3+} species in NiFe LDH [44]. The high-resolution spectrum of O 1 s was deconvoluted into four peaks representing the metal–oxygen bonds (M−O, 528.9 eV), metal-surface hydroxyl bond (M−OH, 529.7 eV), surface adsorbed water (H_2O, 530.5 eV) and intercalated anions ($M-CO_3^{2-}$, 531.6 eV) [38]. In the high-resolution C 1 s spectrum, three absorption peaks are observed at a binding energy of 284.9, 286.0, and 288.3 eV, representing C–C, C–O, and O-C=O, respectively. The presence of O-C=O is ascribed to the intercalated carbonate anion between NiFe LDH nanosheets, which is consistent with the FTIR analysis. The peak of AC absorption at 286.0 eV is due to oxidation of AC on the surface.

4.1.5. Uv–vis analysis

The optical properties of the synthesized AC, NiFe LDH nanosheets and NiFe LDH/AC nanocomposite were determined using the UV–Vis absorption technique, which is illustrated in Fig. 5. As illustrated in Fig. 5**(a),** activated carbon (AC) displays light absorption throughout the

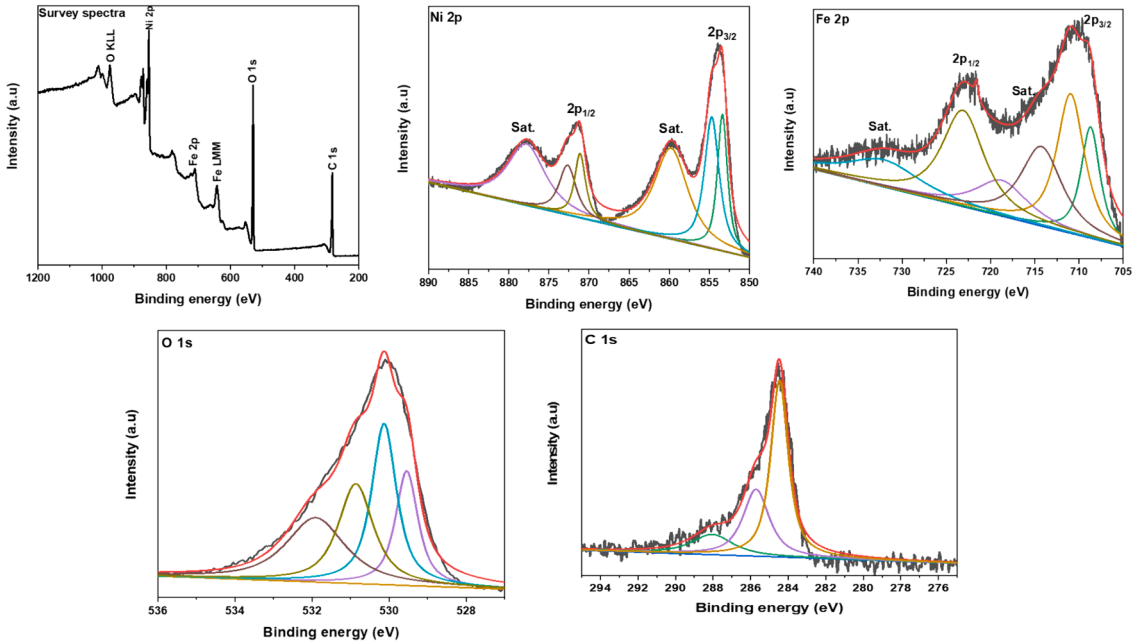

Fig. 4. XPS analysis: Survey spectrum and high-resolution XPS spectra of Ni 2p, Fe 2p, O 1 s, and C 1 s.

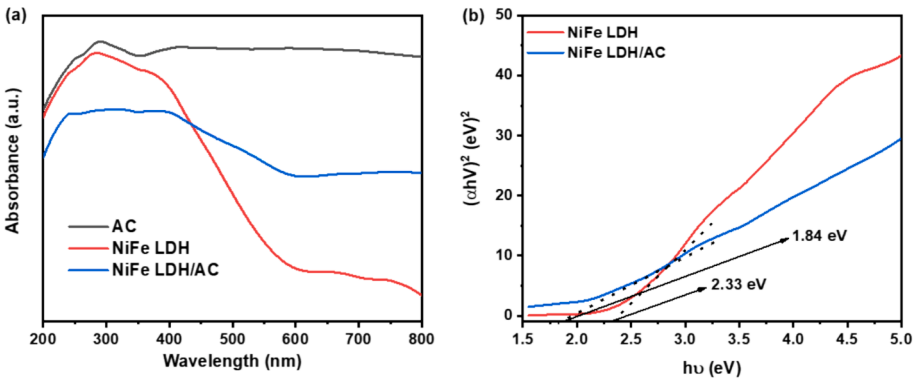

Fig. 5. (a) UV–Vis absorption spectra and (b) Tauc plots for the AC, NiFe LDH nanosheets, and NiFe LDH/AC nanocomposite.

entire spectrum. In contrast, NiFe LDH nanosheets and NiFe LDH/AC nanocomposite exhibit significant bands in the visible spectrum as well as robust absorption in the UV range (200–400 nm). UV light absorption bands are attributed to electron transfers from ligands to metals in an octahedral environment. On the other hand, the broad bands in the 600–800 nm range can be associated with d-d transitions of the metals that make up the layers [45]. Furthermore, the optical band gap of synthesized NiFe LDH nanosheets and the NiFe LDH/AC nanocomposite were estimated to be 2.33 eV and 1.84 eV, respectively, using Tauc plots as shown in Fig. 5**(b)**.

4.1.6. Electrochemical analysis

As shown in **Fig. S2 (a),** cyclic voltammetry (CV) exhibits anodic and cathodic peaks for each of the samples, which indicates high current density and an accelerated electron transference in the NiFe LDH/AC nanocomposite compared to AC and NiFe LDH [46]. The redox reaction of Na^+ in the electrolyte is responsible for the observed peaks of oxidation and reduction in the cyclic voltammogram. For each composite, the anodic and cathodic peaks in the CV demonstrate the current density of the redox reaction of Na^+, which shows accelerated electron transport between the electrolyte and electrode interface [47]. The current density versus potential measurement plot is represented in Fig. S2**(b)** by using the linear sweep voltammetry (LSV) study for the as-synthesized composites/electrodes using AC, NiFe LDH, and NiFe LDH/AC. The current density of AC and NiFe LDH, whose maximum current density is in the voltage range of 0.2–1.0 V, is relatively small [48]. However, the current density of the NiFe LDH/AC composite increases about twice that of the AC and NiFe LDH at 1.0 V voltage after the surface grafting of the NiFe LDH nanosheets onto the AC, indicating that more photoinduced electrons are transferred to the opposite electrode via the external circuit NiFe LDH/AC nanomaterials. In the electrochemical impedance spectroscopy (EIS) Nyquist plot Fig. S2**(c)**, the smallest arc radius was obtained for NiFe LDH/AC compared to AC and NiFe LDH. The reduced diameter observed in the EIS plot for NiFe LDH/AC indicates a lower charge-transfer resistance. This implies enhanced conductivity and more efficient charge transfer within the heterojunction. The results therefore support the conclusion that combining NiFe LDH with AC into a NiFe LDH/AC heterojunction scheme contributes to the enhancement of the charge transfer capacity.

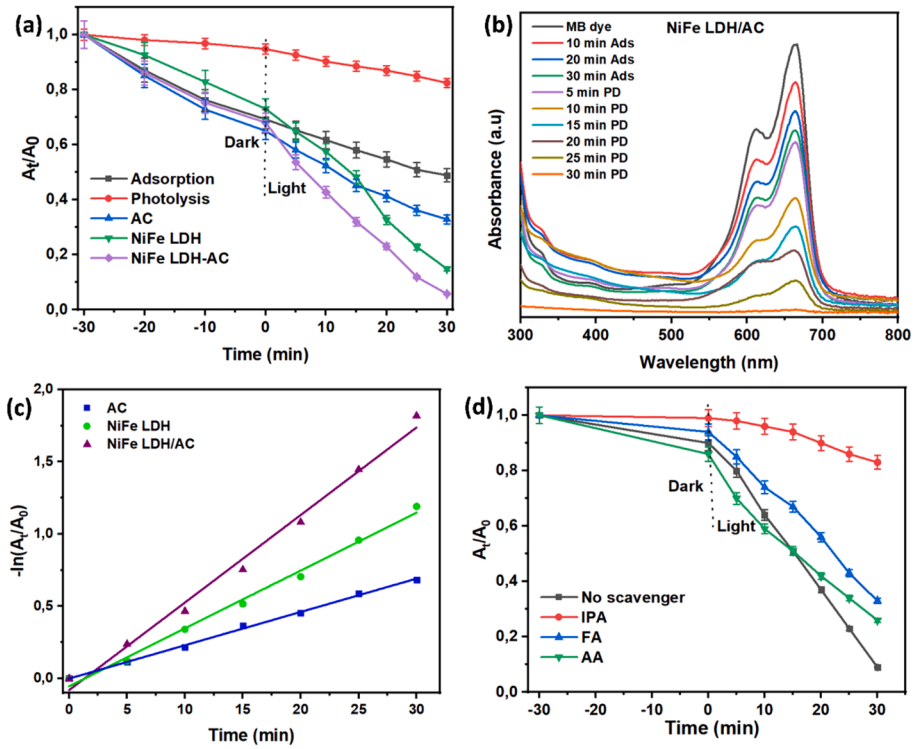

Fig. 6. Photocatalytic activities: (a) Removal rates, (b) NiFe LDH/AC degradation profile, (c) Kinetics study, (d) Effect of radical scavengers.

4.2. Adsorption-photocatalysis results

4.2.1. Adsorption-photodegradation of the MB dye molecule

The absorption spectra of the MB solution during the adsorption and photocatalysis experiments are depicted in Fig. 6. As evident from Fig. 6 **(a)**, the removal efficiency of MB increases as the exposure time increases. The calculated removal rates of MB dye were found to be 17.5 %, 51.2 %, 67.1 %, 84.8 %, and 94.2 % due to photolysis, adsorption, and photocatalysis using AC, NiFe LDH nanosheets, and NiFe LDH/AC nanocomposite, respectively. The photolysis experiment demonstrates the significance of the light source towards the degradation of MB. In contrast, adsorption studies showed that the materials were able to adsorb MB dye in the absence of irradiated light. Based on the photolysis and adsorption experiments, it can be concluded that both the light and catalyst play a significant role during photocatalysis. Fig. 6**(b)** depicts the degradation profile of MB in the presence of NiFe LDH/AC nanocomposite, and it was observed that the major absorption peak of MB (at 664 nm) decreases as the irradiation time increases, signifying the removal of the MB dye.

To further study the kinetics of synthesized catalysts over the photocatalytic degradation of MB dye, the experimental data were fitted to the first-order equation, as shown in Fig. 6**(c)**. The linear conformation supports the pseudo-first-order nature of the kinetic curves. The degradation reaction rate constants were 0.0231, 0.0400, and 0.0606 min^{-1} for AC, NiFe LDH nanosheets, and NiFe LDH/AC nanocomposite, respectively. The rate constant of NiFe LDH/AC nanocomposites is found to be 2.6 and 1.5-fold higher than that of NiFe LDH and AC, respectively. A series of scavenging agents was examined to determine the principal active species responsible for MB degradation (Fig. 6**(c)**). The study also examined the effect of a radical scavenger to apprehend the MB degradation mechanism. Radical scavengers such as ascorbic acid (AA), formic acid (FA), and isopropanol (IPA) were used to capture superoxide radicals ($O_2^{\bullet-}$), holes (h^+), and hydroxyl radicals (•OH), respectively. The maximum photodegradation was observed in the absence of scavengers. The photocatalytic activity was slightly reduced when FA and AA were added to the solution, suggesting that the hole and superoxide radical had little effect. Photodegradation was significantly reduced by the addition of IPA, demonstrating that hydroxyl radicals were the predominant ROS species.

4.2.2. Reusability and stability studies

According to reports, the stability and recyclability of the catalyst are crucial for photocatalysis processes [49]. Reusability studies were carried out to investigate the recyclability of the as-synthesized NiFe LDH/AC nanocomposite in the removal of the MB dye solution. As shown in Fig. S3**(a)**, after five cycles, MB's photodegradation efficiency drops by 20.8 %. The decrease in efficiency can be attributed to the blockage of active sites for both adsorption and photodegradation by the pollutant. Furthermore, to authenticate the stability of the synthesized NiFe LDH/AC nanocomposite, the FTIR and XRD analysis of NiFe LDH/AC were examined before and after MB degradation, and the results are demonstrated in **Fig. S3(b-c)**. The rise of new functional groups on the surface of the synthesized sample was observed from FTIR analysis at around 1600 cm^{-1} (Fig. S3**(b)**). The emergence of those functional groups can be attributed to the absorption of MB dye molecules on the surface of the sample, which blocks the surface-active sites of the sample and results in a decrease in the number of active sites for degradation. The crystal structure of the sample after 5 cycles remained unchanged, as evident from the XRD spectrum (Fig. S3**(c)**). This characteristic demonstrates that the synthesized NiFe LDH/AC nanocomposite possesses high stability.

4.2.3. Proposed photocatalytic degradation mechanism

The degradation mechanism of MB in the presence of NiFe LDH supported on activated carbon (AC) is elucidated in Fig. 7. NiFe LDH and NiFe LDH/AC have narrow band gap energies of 2.33 eV and 1.84 eV,

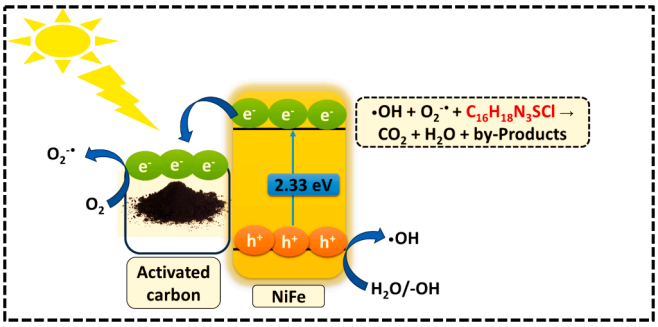

Fig. 7. Probable degradation mechanism of MB using NiFe LDH/AC.

respectively, implying that these photocatalytic materials can be excited by visible light irradiation. As a result of visible light irradiation, photoexcited e^- migrates from the valance band (VB) to the conduction band (CB) of NiFe LDH, while the h^+ in the VB remains still, as depicted in Equation (6). However, it is more likely that the small band gap energy of NiFe LDH will cause rapid recombination of e^- and h^+ pairs and, ultimately, lead to low photocatalytic efficiency. Therefore, in this study, NiFe LDH was supported on activated carbon as an electron acceptor and photoexcited charge carrier to retard a high rate of recombination. Therefore, the photoexcited electrons in the CB of NiFe LDH are transferred to the CB of activated carbon. At the same time, the h^+ in the VB of NiFe remains in the VB, thus providing better charge separation and suppressing the recombination of e^-/h^+ pairs, as shown in Equations (6–7).

Meanwhile, excited e^- in activated carbon (AC) CB can react with adsorbed O_2 on the surface and form superoxide radicals ($O_2^{\bullet-}$) since the CB band potential (−1.14 V vs NHE) of AC is more negative than the reduction potential of O_2 / O_2^- • of −0.33 V vs NHE, as shown in Equation (8) [50]. On the contrary, e^- in the CB of NiFe LDH cannot reduce the adsorbed O_2 molecules on the surface to produce superoxide radicals ($O_2^{\bullet-}$) due to the weak CB potential (−0.31 V vs NHE) of NiFe LDH compared to O_2 / O_2^- • (−0.33 V vs NHE) [44]. Meanwhile, h^+ in the VB of NiFe LDH oxidizes adsorbed water molecules (H_2O) and –OH species to generate hydroxyl radicals (•OH) since NiFe LDH has stronger CB potential (2.55 V vs NHE) than that of •OH/–OH (2.27 V vs NHE) as shown in Equation (9) [51]. Subsequently, the VB potential of AC (1.56 V vs NHE) is less positive for oxidization • OH / –OH (2.27 V vs NHE), therefore, oxidation H_2O cannot occur on the surface of AC [50]. The probable degradation mechanism is illustrated in Fig. 7. The presence of these reactive radicals (•OH and $O_2^{\bullet-}$) was responsible for the decomposition of MB and was consistent with the analysis from the effect of scavengers, revealing that •OH was the major reactive species towards the degradation of MB into simpler compounds such as H_2O, CO_2, and other by-products as recorded in Equation (10). In summary, the exploitation of the synergetic effect between NiFe LDH, which provides catalytic activities, and AC, which provides plenty of surface area for MB dye to attach, and subsequently led to better remediation of MB dye, and ultimately, these catalysts can be considered as a promising material for future water treatment technologies. The proposed reactions were as follows:

$$\text{NiFe LDH} + h\nu \rightarrow \text{NiFe LDH } (h^+_{VB} + e^-_{(CB)}) \quad (6)$$

$$\text{NiFe LDH } (h^+_{VB} + e^-_{(CB)}) + \text{AC} \rightarrow \text{NiFe LDH } (h^+_{VB}) + \text{AC } (e^-_{(CB)}) \quad (7)$$

$$\text{AC } (e^-_{(CB)}) + O_2 \rightarrow O_2^{\bullet-} \quad (8)$$

$$h^+_{(VB)} + H_2O \rightarrow \bullet OH + H^+ \quad (9)$$

$$\bullet OH + O_2^{\bullet-} + \text{MB dye} \rightarrow CO_2 + H_2O + \text{by-products} \quad (10)$$

4.2.4. Possible degradation pathway of MB using UPLC/MS

The photocatalytic degradation of MB in an aqueous environment was evaluated using a NiFe/AC photocatalyst in the presence of UV–visible light and elucidated using UPLC/MS. More than 8 major degraded products were reached and identified due to MB decomposition through UPLC/MS analysis after 30 min of UV–visible-light irradiation (**Fig. S4**(a-d)). The mass spectra (**Fig. S4**(c-d)) were operated in the positive ionization mode and showed various degraded products with their mass-to-charge (*m/z*) ratios as follows 303, 216, 202, 188, 173, 158, 110, and 94 *m/z*. Through the help of the previously reported literature, the degraded products in the mass spectra emanating from MB degradation that were obtained were correlated with the previous studies. Subsequently, the degradation pathway for MB was predicted, as depicted in Fig. 8 [52,53]. The prominent peak in the mass spectra with the *m/z* ratio of 284 (in the absence of Cl^-) was identified as the MB peak appearing at the retention time of 4.50 min in the chromatogram (**Fig. S4**(a-b)). Subsequently, after 30 min of UV–visible light irradiation, eight (8) degradation products, namely, 1,1′-sulfinyldibenzene (P1 = 202 *m/z*), (P2 = 2-[3-(dimethylamino)benzene-1-sulfinyl]-*N,N*-dimethylbenzene-1,4-diamine), benzenesulfonic acid (P3 = 158 *m/z*), 2-amino-5-(dimethylamino)benzene-1-sulfonic acid (P4 = 216 *m/z*), benzene-1,2-diol (P5 = 110 *m/z*), 2,5-diaminobenzene-1-sulfonic acid (P6 = 188 *m/z*), phenol (P7 = 94 *m/z*), and 2-aminobenzene-1-sulfonic acid (P8 = 173 *m/z*) were obtained. The formation of those products was caused first by the transfer of electrons from the catalyst to the electrophilic nitrogen atom in the MB, thus forming leucomethylene blue with 287 *m/z*. Thereafter, a series of chemical reactions including, protonation, hydroxylation, and sulfur oxidation on leucomethylene blue led to the formation of nitrated products, sulfone group, and phenyl ring opening, among other products. In essence, during the photodegradation of MB, the –OH radicals and h^+ tend to target the chromophore center, causing cleavage in the amino group, hydroxylation, dealkylation, dehydration, protonation and demethylation of the phenyl groups, and thus generating different products (P1-P8). The final products of MB degradation include smaller products such as H_2O, CO_2, SO_4^-, and NO_3. Based on the UPLC/MS analysis, the plausible photodegradation pathway of MB was proposed, as shown in Fig. 8**.**

4.2.5. Application of NiFe LDH/AC for the degradation of MB in textile wastewater

Under optimum conditions, the maximum degradation efficiency of 90.53 % and 92.18 % was achieved for NiFe LDH/AC under a visible light source for 30 min in the upstream and downstream rivers, respectively (Table 2**)**. However, in wastewater, the maximum degradation efficiency was 85.14 % and 87.44 % in influent textile wastewater and effluent textile wastewater, respectively (Table 2**)**. This enhanced activity can be attributed to the synergistic interactions of NiFe LDH and AC through the advanced oxidation process (AOP) when the time was varied. The high degradation efficiencies indicate that there were no possible interfering substances in the form of other

Table 2
Application of NiFe LDH/AC on the degradation of MB in influent textile wastewater and effluent textile wastewater, as well as river water near the textile industry.

Samples	Absorbance before degradation	Absorbance after degradation	% Degraded
Influent	1.353	0.201	85.14
Effluent	1.123	0.141	87.44
Upstream	1.067	0.101	90.53
Downstream	1.011	0.079	92.18

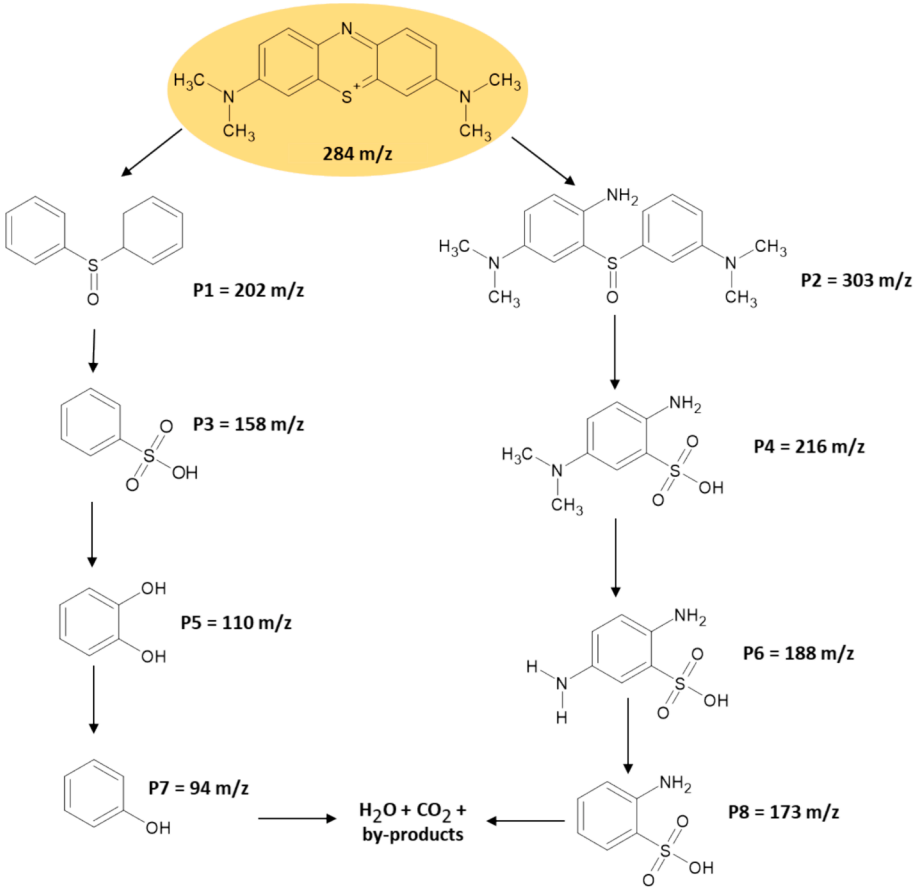

Fig. 8. Possible mechanism of MB degradation in the presence of NiFe LDH/AC photocatalyst using UPLC/MS.

components within the wastewater matrices that could limit the degradation of MB. The performance of the NiFe LDH/AC was compared with different materials that were reported for the degradation of MB (Table S2). NiFe LDH/AC composite demonstrated high degradation efficiencies compared to most reported materials for the degradation of MB. This could be ascribed to synergistic proportions of the integration of NiFe LDH with AC that led to abundant surface-active sites and high conductivity that could influence the transfer of electrons and generation of holes responsible for the oxidative and reductive radicals for the extensive degradation of MB.

5. Conclusion

In summary, heterojunction structures between NiFe LDH nanosheets and tyre-waste derived activated carbon were synthesized for their application in the adsorption-photocatalytic remediation of methylene blue dye in an aqueous solution. The attained data signifies that waste tyre can be utilized to fabricate activated carbon as an active adsorbent and support material for catalysts for the eradication of baneful wastewater pollutants. Thus, a comprehensive characterization study confirmed the successful attainment of the NiFe LDH/AC nanocomposites. The prepared NiFe LDH/AC nanocomposite exhibits excellent adsorption-photocatalytic performance under visible light illumination with a total MB remediation efficiency of 94.2 % attained in 30 min. Such superior performance is mainly ascribed to the synergistic effect between NiFe LDH and activated carbon in terms of enhancement separation and transfer of photogenerated charge carriers. A radical scavenger test reveals that hydroxyl radicals contribute the most to the removal of MB. Furthermore, the NiFe LDH/AC photocatalyst exhibits excellent recyclability and good stability. The probable mechanism of MB degradation with the photocatalyst was understood from a series of tests on the intermediates in the process. Under optimum conditions, the NiFe LDH/AC composite could remove 85–87 % of MB from textile wastewater and 90–92 % of MB in river water samples collected near a textile industrial park. Therefore, the NiFe LDH/AC nanocomposite is a good candidate for removing organic pollutants such as dyes from industrial textile wastewater. Furthermore, the disposal of non-biodegradable scrap tyres is causing environmental and health challenges that affect humans, and aquatic organisms. Hence, innovative technologies (such as the production of activated carbon) that can assist in converting waste tyres into valuable products are imperative and should be encouraged to minimize waste in the environment. Developing large-scale production of waste tyre-derived activated carbon is attractive, which is comparably cheaper and sustainable considering the abundance of raw material (worn-out tyres) that is disposed of in various specialized plants and industries. This process also offers an additional superiority over other carbon materials such as high surface area, large porosity, rapid adsorption rate, remarkable reusability, and recyclability activities, which are desired for large-scale water treatment applications.

6. Author contribution statement

Tshimangadzo S. Munonde: Conceived and designed the experiments; Performed the experiments; Analyzed and interpreted the data; Contributed reagents, materials, analysis tools or data; Wrote the paper. **Ntakadzeni Madima**: Conceived and designed the experiments; Performed the experiments; Analyzed and interpreted the data, Wrote the paper. **Rudzani Ratshiedana**: Conceived and designed the experiments; Performed the experiments; Contributed reagents, materials, analysis tools or data, Wrote the paper. **Lethula E. Mofokeng**: Performed the experiments; Analyzed and interpreted the data; Contributed reagents, materials, analysis tools or data; Wrote the paper. **Ratshilumela S. Dima**: Conceived and designed the experiments; Analyzed and interpreted the data; Contributed reagents, materials, analysis tools or data; Reviewed the paper. **Philiswa N. Nomngongo**: Conceived and designed the experiments; Analyzed and interpreted the data; Contributed reagents, materials, analysis tools or data; Reviewed the paper.

7. Funding statement

Financial support received from the Department of Science and Innovation-National Research Foundation South African Research Chairs Initiative (DSI-NRF SARChI) (grant no. 91230) and the University of South Africa is acknowledged.

CRediT authorship contribution statement

Tshimangadzo S. Munonde: Writing – original draft, Validation, Resources, Project administration, Methodology, Investigation, Formal analysis, Data curation, Conceptualization. **Ntakadzeni Madima:** Writing – original draft, Visualization, Validation, Methodology, Investigation, Formal analysis, Conceptualization. **Rudzani Ratshiedana:** Writing – original draft, Visualization, Validation, Resources, Methodology, Investigation, Formal analysis, Data curation, Conceptualization. **Philiswa Nosizo Nomngongo:** Writing – review & editing, Visualization, Software, Resources, Investigation, Funding acquisition, Conceptualization. **Lethula E. Mofokeng:** . **Ratshilumela S. Dima:** Writing – review & editing, Visualization, Validation, Software, Methodology, Investigation, Conceptualization.

Declaration of competing interest

The authors declare that they have no known competing financial interests or personal relationships that could have appeared to influence the work reported in this paper.

Data availability

Data will be made available on request.

Acknowledgments

The authors wish to thank the Institute for Nanotechnology and Water Sustainability (iNanoWS) of the University of South Africa, Mintek, CSIR, University of Johannesburg and University of Pretoria for their support through facilities used in this study.

Appendix A. Supplementary data

Supplementary data to this article can be found online at https://doi.org/10.1016/j.apsusc.2024.161205.

References

[1] K. Obaideen, N. Shehata, E.T. Sayed, M.A. Abdelkareem, M.S. Mahmoud, A. G. Olabi, The role of wastewater treatment in achieving sustainable development goals (SDGs) and sustainability guideline, Energy Nexus 7 (2022) 100112, https://doi.org/10.1016/j.nexus.2022.100112.

[2] S. Roy, R. Rautela, S. Kumar, Towards a sustainable future: Nexus between the sustainable development goals and waste management in the built environment, J. Clean. Prod. 415 (2023) 137865, https://doi.org/10.1016/j.jclepro.2023.137865.

[3] N. Shehata, D. Egirani, A.G. Olabi, A. Inayat, M.A. Abdelkareem, K.J. Chae, E. T. Sayed, Membrane-based water and wastewater treatment technologies: Issues, current trends, challenges, and role in achieving sustainable development goals, and circular economy, Chemosphere 320 (2023) 137993, https://doi.org/10.1016/j.chemosphere.2023.137993.

[4] C. Garcia-Saravia Ortiz-de-Montellano, P. Samani, Y. van der Meer, How can the circular economy support the advancement of the Sustainable Development Goals (SDGs)? A comprehensive analysis, Sustain. Prod. Consum. 40 (2023) 352–362, https://doi.org/10.1016/j.spc.2023.07.003.

[5] P. Yang, Y. Lu, H. Zhang, R. Li, X. Hu, A. Shahab, A.Y. Elnaggar, A.F. Alrefaei, M. H. Almutairil, E. Ali, Effective removal of methylene blue and crystal violet by low-cost biomass derived from eucalyptus: Characterization, experiments, and mechanism investigation, Environ. Technol. Innov. 33 (2024) 103459, https://doi.org/10.1016/j.eti.2023.103459.

[6] M. Bashir, M. Batool, N. Arif, M. Tayyab, Y.J. Zeng, M. Nadeem Zafar, Strontium-based nanomaterials for the removal of organic/inorganic contaminants from water: A review, Coord. Chem. Rev. 492 (2023) 215286, https://doi.org/10.1016/j.ccr.2023.215286.

[7] S. Majumder, B. Dhara, A.K. Mitra, S. Dey, Applications and implications of carbon nanotubes for the sequestration of organic and inorganic pollutants from wastewater, Environ. Sci. Pollut. Res. 30 (2023) 124934–124949, https://doi.org/10.1007/s11356-023-25431-9.

[8] U. Basharat, W. Zhang, M.Y. Jat Baloch, A. Abbasi, B.A. Khan, S. Mahroof, S. H. Khan, A. Niaz, M. Irshad, Presence and Dispersion of Organic and Inorganic Contaminants in Groundwater, Sustain. Environ. 8 (2023) p71, https://doi.org/10.22158/se.v8n3p71.

[9] S. Muzammal, A. Ahmad, M. Sheraz, J. Kim, S. Ali, M.B. Hanif, I. Hussain, S. Pandiaraj, A. Alodhayb, M.S. Javed, H.A.Z. Al-bonsrulah, M. Motola, Polymer-supported nanomaterials for photodegradation: UnPraveling the methylene blue menace, Energy Convers. Manag. X 22 (2024) 100547, https://doi.org/10.1016/j.ecmx.2024.100547.

[10] E.M. Abd El-Monaem, A.M. Omer, G.M. El-Subruiti, M.S. Mohy-Eldin, A. S. Eltaweil, Zero-valent iron supported-lemon derived biochar for ultra-fast adsorption of methylene blue, Biomass Convers, Biorefinery 14 (2024) 1697–1709, https://doi.org/10.1007/s13399-022-02362-y.

[11] S. Modi, V.K. Yadav, A. Gacem, I.H. Ali, D. Dave, S.H. Khan, K.K. Yadav, S. U. Rather, Y. Ahn, C.T. Son, B.H. Jeon, Recent and Emerging Trends in Remediation of Methylene Blue Dye from Wastewater by Using Zinc Oxide Nanoparticles, Water (switzerland) 14 (2022), https://doi.org/10.3390/w14111749.

[12] H.S. Kusuma, D.E. Christa Jaya, N. Illiyanasafa, K.L. Ikawati, E. Kurniasari, H. Darmokoesoemo, A.N. Amenaghawon, A critical review and bibliometric analysis of methylene blue adsorption using leaves, Chemosphere 356 (2024) 141867, https://doi.org/10.1016/j.chemosphere.2024.141867.

[13] P. Mandal, J. Debbarma, M. Saha, Critical Review on the Photodegradation Ability of Graphene and its Derivatives against Malachite Green, Methylene Blue, and Methyl Orange, Lett. Appl. Nanobioscience 12 (2023), https://doi.org/10.33263/LIANBS121.006.

[14] F. Mashkoor, A. Nasar, Magsorbents: Potential candidates in wastewater treatment technology – A review on the removal of methylene blue dye, J. Magn. Magn. Mater. 500 (2020) 166408, https://doi.org/10.1016/j.jmmm.2020.166408.

[15] S. Ihaddaden, D. Aberkane, A. Boukerroui, D. Robert, Removal of methylene blue (basic dye) by coagulation-flocculation with biomaterials (bentonite and Opuntia ficus indica), J. Water Process Eng. 49 (2022) 102952, https://doi.org/10.1016/j.jwpe.2022.102952.

[16] M.A. Pathirana, N.S.L. Dissanayake, N.D. Wanasekara, B. Mahltig, G.K. Nandasiri, Chitosan-Graphene Oxide Dip-Coated Polyacrylonitrile-Ethylenediamine Electrospun Nanofiber Membrane for Removal of the Dye Stuffs Methylene Blue and Congo Red, Nanomaterials 13 (2023), https://doi.org/10.3390/nano13030498.

[17] A.A. Adesibikan, S.S. Emmanuel, C.O. Olawoyin, P. Ndungu, Cellulosic metallic nanocomposites for photocatalytic degradation of persistent dye pollutants in aquatic bodies: A pragmatic review, J. Organomet. Chem. 1010 (2024) 123087, https://doi.org/10.1016/j.jorganchem.2024.123087.

[18] M. Ahtasham Iqbal, S. Akram, S. khalid, B. Lal, S.U. Hassan, R. Ashraf, G. Kezembayeva, M. Mushtaq, N. Chinibayeva, A. Hosseini-Bandegharaei, Advanced photocatalysis as a viable and sustainable wastewater treatment process: A comprehensive review, Environ. Res. 253 (2024) 118947. doi: 10.1016/j.envres.2024.118947.

[19] D. Van Thuan, H.L. Ngo, H.P. Thi, T.T.H. Chu, Photodegradation of hazardous organic pollutants using titanium oxides -based photocatalytic: A review, Environ. Res. 229 (2023) 116000, https://doi.org/10.1016/j.envres.2023.116000.

[20] D.M. Osorio-Aguilar, H.A. Saldarriaga-Noreña, M.A. Murillo-Tovar, J. Vergara-Sánchez, J. Ramírez-Aparicio, L. Magallón-Cacho, M.L. García-Betancourt, Adsorption and Photocatalytic Degradation of Methylene Blue in Carbon Nanotubes: A Review with Bibliometric Analysis, Catalysts 13 (2023), https://doi.org/10.3390/catal13121480.

[21] S. Sonar, J.M. Giraudon, S.K.P. Veerapandian, R. Bitar, K. Leus, P. Van Der Voort, J. F. Lamonier, R. Morent, N. De Geyter, A. Löfberg, Abatement of toluene using a sequential adsorption-catalytic oxidation process: Comparative study of potential adsorbent/catalytic materials, Catalysts 10 (2020) 1–20, https://doi.org/10.3390/catal10070761.

[22] K.P. Gopinath, N.V. Madhav, A. Krishnan, R. Malolan, G. Rangarajan, Present applications of titanium dioxide for the photocatalytic removal of pollutants from water: A review, J. Environ. Manage. 270 (2020) 110906, https://doi.org/10.1016/j.jenvman.2020.110906.

[23] A.A. Lugo-Ruiz, M.J. Paz-Ruiz, S.J. Bailón-Ruiz, Degradation of organic dyes in the presence of activated titanium-based nanoparticles, MRS Adv. 7 (2022) 289–294, https://doi.org/10.1557/s43580-021-00144-8.

[24] C. Sivaraman, S. Vijayalakshmi, E. Leonard, S. Sagadevan, R. Jambulingam, Current Developments in the Effective Removal of Environmental Pollutants through Photocatalytic Degradation Using Nanomaterials, Catalysts 12 (2022), https://doi.org/10.3390/catal12050544.

[25] E.D.H. Kong, J.H.F. Chau, C.W. Lai, C.S. Khe, G. Sharma, A. Kumar, S. Siengchin, M.R. Sanjay, GO/TiO_2-Related Nanocomposites as Photocatalysts for Pollutant Removal in Wastewater Treatment, Nanomaterials 12 (2022), https://doi.org/10.3390/nano12193536.

[26] Y. He, R. Yuan, J. Yan, J. Li, A highly efficient NiFe-layer double hydroxide/TiO_2 heterojunction photoanode-based high-performance bifunctional photocatalytic fuel cell, Mater. Today Commun. 26 (2021) 102177, https://doi.org/10.1016/j.mtcomm.2021.102177.

[27] H. You, M. Vinothkannan, S. Shanmugam, Porous lanthanum titanium oxide nanostructure composite membrane to enhance the power output and chemical durability of low-humidifying polymer electrolyte fuel cells: impact of additive morphology, Mater. Today Chem. 32 (2023) 101634, https://doi.org/10.1016/j.mtchem.2023.101634.

[28] C. Lei, M. Pi, P. Kuang, Y. Guo, F. Zhang, Organic dye removal from aqueous solutions by hierarchical calcined Ni-Fe layered double hydroxide: Isotherm, kinetic and mechanism studies, J. Colloid Interface Sci. 496 (2017) 158–166, https://doi.org/10.1016/j.jcis.2017.02.025.

[29] Y. Lu, B. Jiang, L. Fang, F. Ling, J. Gao, F. Wu, X. Zhang, High performance NiFe layered double hydroxide for methyl orange dye and Cr(VI) adsorption, Chemosphere 152 (2016) 415–422, https://doi.org/10.1016/j.chemosphere.2016.03.015.

[30] T. Ma, C. Liu, Z. Li, R. Zheng, M. Chen, S. Dai, T. Zhao, Mechanochemically constructed Bi_2WO_6/Zn-Al layered double hydroxide heterojunction with prominent visible light-driven photocatalytic efficiency, Appl. Clay Sci. 215 (2021) 106328, https://doi.org/10.1016/j.clay.2021.106328.

[31] S. Nayak, K.M. Parida, Deciphering Z-scheme Charge Transfer Dynamics in Heterostructure NiFe-LDH/N-rGO/g-C_3N_4 Nanocomposite for Photocatalytic Pollutant Removal and Water Splitting Reactions, Sci. Rep. 9 (2019) 1–23, https://doi.org/10.1038/s41598-019-39009-4.

[32] D. Tichit, M.G. Álvarez, Layered Double Hydroxide/Nanocarbon Composites as Heterogeneous Catalysts: A Review, ChemEngineering 6 (2022) 1–44, https://doi.org/10.3390/chemengineering6040045.

[33] A. Ali Khan, M. Tahir, N. Khan, LDH-based nanomaterials for photocatalytic applications: A comprehensive review on the role of bi/trivalent cations, anions, morphology, defect engineering, memory effect, and heterojunction formation, J. Energy Chem. 84 (2023) 242–276, https://doi.org/10.1016/j.jechem.2023.04.049.

[34] Z.H. Xie, H.Y. Zhou, C.S. He, Z.C. Pan, G. Yao, B. Lai, Synthesis, application and catalytic performance of layered double hydroxide based catalysts in advanced oxidation processes for wastewater decontamination: A review, Chem. Eng. J. 414 (2021) 128713, https://doi.org/10.1016/j.cej.2021.128713.

[35] K.M. Dimpe, J.C. Ngila, P.N. Nomngongo, Application of waste tyre-based activated carbon for the removal of heavy metals in wastewater, Cogent Eng. 4 (2017), https://doi.org/10.1080/23311916.2017.1330912.

[36] T.S. Munonde, N.P. September, A. Mpupa, P.N. Nomngongo, Two agitation routes for the adsorption of Reactive Red 120 dye on NiFe LDH/AC nanosheets from wastewater and river water, Appl. Clay Sci. 219 (2022) 106438, https://doi.org/10.1016/j.clay.2022.106438.

[37] W. Ahmad, S. Qaiser, R. Ullah, B.M. Jan, M.A. Karakassides, C.E. Salmas, G. Kenanakis, R. Ikram, Utilization of tires waste-derived magnetic-activated carbon for the removal of hexavalent chromium from wastewater, Materials (basel). 14 (2021) 1–18, https://doi.org/10.3390/ma14010034.

[38] T.S. Munonde, H. Zheng, The impact of ultrasonic parameters on the exfoliation of NiFe LDH nanosheets as electrocatalysts for the oxygen evolution reaction in alkaline media, Ultrason. Sonochem. 76 (2021) 105664, https://doi.org/10.1016/j.ultsonch.2021.105664.

[39] H. Hu, S. Wageh, A.A. Al-Ghamdi, S. Yang, Z. Tian, B. Cheng, W. Ho, NiFe-LDH nanosheet/carbon fiber nanocomposite with enhanced anionic dye adsorption performance, Appl. Surf. Sci. 511 (2020) 145570, https://doi.org/10.1016/j.apsusc.2020.145570.

[40] C. Zheng, Z. Xie, T. Li, S. Wei, B. Liu, H. Liu, R. Suo, J. Wen, Y. Xie, Y. Lin, C. Lu, Surface-induced strategy: Phosphorus-induced NiFe-LDH generation of strong surface bonding states for efficient photocatalytic hydrogen evolution, Appl. Surf. Sci. 657 (2024) 159789, https://doi.org/10.1016/j.apsusc.2024.159789.

[41] J. Ren, H. Weng, B. Li, F. Chen, J. Liu, Z. Song, The Influence Mechanism of Pore Structure of Tectonically Deformed Coal on the Adsorption and Desorption Hysteresis, Front, Earth Sci. 10 (2022) 1–16, https://doi.org/10.3389/feart.2022.841353.

[42] M.T.Q.S. da Silva, F. Perretto, M. do Rocio Cardoso, W. Mazer, Porosity: Some characterization techniques, Mater. Today Proc. (2023). doi: 10.1016/j.matpr.2023.03.716.

[43] T.S. Munonde, H. Zheng, P.N. Nomngongo, Ultrasonic exfoliation of NiFe LDH/CB nanosheets for enhanced oxygen evolution catalysis, Ultrason. Sonochem. 59 (2019) 104716, https://doi.org/10.1016/j.ultsonch.2019.104716.

[44] J. Yan, X. Zhang, W. Zheng, L.Y.S. Lee, Interface Engineering of a 2D–C_3N_4/NiFe-LDH Heterostructure for Highly Efficient Photocatalytic Hydrogen Evolution, ACS Appl. Mater. Interfaces (2021), https://doi.org/10.1021/acsami.1c03240.

[45] M.Á. Oliva, D. Giraldo, P. Almodóvar, F. Martín, M.L. López, I. Pavlovic, L. Sánchez, Designing a NiFe-LDH/MnO_2 heterojunction to improve the photocatalytic activity for NOx removal under visible light, Chem. Eng. J. 489 (2024) 151241, https://doi.org/10.1016/j.cej.2024.151241.

[46] C. Han, Z. Chen, N. Zhang, J.C. Colmenares, Y.J. Xu, Hierarchically CdS decorated 1D ZnO nanorods-2D graphene hybrids: Low temperature synthesis and enhanced photocatalytic performance, Adv. Funct. Mater. 25 (2015) 221–229, https://doi.org/10.1002/adfm.201402443.

[47] L. Peng, C. Yu, Y. Ma, G. Xie, X. Xie, Z. Wu, N. Zhang, Self-assembled transition metal chalcogenides@CoAl-LDH 2D/2D heterostructures with enhanced photoactivity for hydrogen evolution, Inorg. Chem. Front. 9 (2022) 994–1005, https://doi.org/10.1039/d1qi01603b.

[48] H. Huang, X. Jiang, N. Li, D. Chen, Q. Xu, H. Li, J. He, J. Lu, Noble-metal-free ultrathin MXene coupled with In_2S_3 nanoflakes for ultrafast photocatalytic

reduction of hexavalent chromium, Appl. Catal. B Environ. 284 (2021) 119754, https://doi.org/10.1016/j.apcatb.2020.119754.
[49] N. Madima, K.K. Kefeni, A.T. Kuvarega, S.B. Mishra, A.K. Mishra, Visible-light-driven Z-scheme ternary $Fe_3O_4/TiO_2/g\text{-}C_3N_4$ nanocomposite as reusable photocatalyst for efficient removal of dyes and chromium in water, Mater. Chem. Phys. 296 (2023) 127233, https://doi.org/10.1016/j.matchemphys.2022.127233.
[50] J. Hemalatha, M. Senthil, D. Madhan, A.M. Al-Mohaimeed, W.A. Al-onazi, Fabrication of $NiFe_2O_4$ nanoparticles loaded on activated carbon as novel composites for high efficient ultra violet-light photocatalysis for degradation of aqueous organic pollutants, Diam. Relat. Mater. 144 (2024) 110995, https://doi.org/10.1016/j.diamond.2024.110995.
[51] Z. Mohammadi, H. Abbasi-Asl, M.M. Sabzehmeidani, M. Ghaedi, Z. Moradi, Interface engineering of a magnetic 2D–C_3N_4/Fe_2O_3/NiFe-LDH heterostructure for efficient photocatalytic degradation of methylene blue and rhodamine B dyes under visible light, Appl. Clay Sci. 246 (2023) 107182, https://doi.org/10.1016/j.clay.2023.107182.
[52] J. Lin, Z. Luo, J. Liu, P. Li, Photocatalytic degradation of methylene blue in aqueous solution by using ZnO-SnO_2 nanocomposites, Mater. Sci. Semicond. Process. 87 (2018) 24–31, https://doi.org/10.1016/j.mssp.2018.07.003.
[53] C.H. Nguyen, C.C. Fu, R.S. Juang, Degradation of methylene blue and methyl orange by palladium-doped TiO_2 photocatalysis for water reuse: Efficiency and degradation pathways, J. Clean. Prod. 202 (2018) 413–427, https://doi.org/10.1016/j.jclepro.2018.08.110.